

# Plasmonic nose : integrating the MOF-enabled molecular preconcentration effect with a plasmonic array for recognition of molecular-level volatile organic compounds

Koh, Charlynn Sher Lin; Lee, Hiang Kwee; Han, Xuemei; Sim, Howard Yi Fan; Ling, Xing Yi

2018

Koh, C. S. L., Lee, H. K., Han, X., Sim, H. Y. F., & Ling, X. Y. (2018). Plasmonic nose: integrating the MOF-enabled molecular preconcentration effect with a plasmonic array for recognition of molecular-level volatile organic compounds. *Chemical Communications*, 54(20), 2546-2549. doi:10.1039/C8CC00564H

<https://hdl.handle.net/10356/90134>

<https://doi.org/10.1039/C8CC00564H>

---

© 2018 The Author(s). All rights reserved. This paper was published by The Royal Society of Chemistry in *Chemical Communications* and is made available with permission of The Author(s).

*Downloaded on 20 Mar 2024 17:26:10 SGT*



Journal Name

## COMMUNICATION

# Plasmonic Nose: Integrating MOF-enabled Molecular Preconcentration with Plasmonic Array for Molecular-level Volatile Organic Compounds Recognition

Received 00th January 20xx,  
Accepted 00th January 20xx

DOI: 10.1039/x0xx00000x

www.rsc.org/

Charlynn Sher Lin Koh,<sup>a</sup> Hiang Kwee Lee,<sup>a,b</sup> Xuemei Han,<sup>a</sup> Howard Yi Fan Sim,<sup>a</sup> and Xing Yi Ling<sup>\*a</sup>

**Timely detection of toxic vapor is vital in safeguarding people's lives. Herein, we design a plasmonic nose based on zeolitic imidazolate framework (ZIF)-encapsulated Ag nanocubes array for ultratrace recognition of VOCs vapor. The plasmonic nose enables in-situ adsorption kinetics and recognition of various VOCs at ppm levels, eliminating false-positives. Our approach provides a paradigm shift as next-generation, effective and specific gas sensor.**

Toxins are most potent in the vapor form as they can readily access our respiratory system to cause instantaneous harm even at the ppm level.<sup>1</sup> However, human olfactory systems are often inept at discerning these lurking dangers owing to limited sensitivity. To maintain environmental and industrial safety, surface-enhanced Raman scattering (SERS) spectroscopy-based sensor emerges as a powerful gas detection technique by offering molecular-specific information even at trace concentration.<sup>2</sup> Notably, these SERS-based sensors also address the limitations of commercial gas sensing devices<sup>3</sup> such as high quantification limit, long response time and/or susceptibility to false positive response due to the lack of molecular specificity/recognition. Furthermore, SERS also surpasses other analytical methods such as surface plasmon resonance or refractive index which mostly depend on indirect physical changes and cannot provide molecular structure information.<sup>4</sup> These multitude of benefits potentially allows SERS-based platforms to function as a 'plasmonic nose', capable of "sniffing" out gas components at the molecular-level with

sensitivity far surpassing that of human's nose. Despite the immense potential, current SERS-based gas detection must be coupled with additional pre-treatment system such as thermoelectric cooler to condense gas onto the analytical platform. Direct gas detection remains a challenge due to their low concentrations and poor affinity to the plasmonic-active surface.

The integration of metal-organic frameworks (MOFs) with SERS overcomes these limitations because MOFs can confine gas molecules directly at the SERS-active surfaces, even in the absence of gas condenser or specific gas-surface affinity. This imparts molecular preconcentration effect that greatly enhance SERS performance, allowing the detection of molecules down to femtomolar level.<sup>5-7</sup> Thus far, most MOF-based SERS systems are utilized for aqueous/liquid sensing applications, while gas detection is still non-trivial due to poor plasmonic enhancements and background interference problems. Such limitations arise from the typical use of impregnation-based particle synthesis, which is difficult to control particle size, shape and density for optimal SERS activities. More importantly, a critical drawback from all current methods is that they only focus on gas adsorption using MOFs, which alone do not fully utilize the 3D spatial field enhancements and is insufficient to tackle the pressing sensitivity issue. A multifaceted approach to overcome MOF-SERS performance bottleneck is therefore required for sensitive and rapid molecular-level readout in practical vapor detections, and in kinetic studies involving gas molecules.

Herein, we design a plasmonic nose based on a zeolitic imidazolate framework (ZIF)-encapsulated Ag nanocube platform (Ag@ZIF) to concentrate both gas molecules and electromagnetic (EM) field at the nanometer-scale in three-dimensional (3D) space, achieving ultratrace SERS detection of non-adsorbing volatile organic compounds (VOCs) down to ppm level. Our plasmonic nose consists of multifaceted strategies to achieve low gas detection limit – (1) optimizing the effective preconcentration of gas, and (2) intensifying EM hotspots by manipulating plasmonic coupling between adjacent Ag

<sup>a</sup> C.S.L. Koh, Dr. H.K. Lee, Dr. X. Han, H.Y.F. Sim, Prof X.Y. Ling  
Division of Chemistry and Biological Chemistry,  
School of Physical and Mathematical Sciences  
Nanyang Technological University  
21 Nanyang Link, Singapore 637371  
E-mail: [xyling@ntu.edu.sg](mailto:xyling@ntu.edu.sg)

<sup>b</sup> Dr. H.K. Lee  
Institute of Materials Research and Engineering  
Agency for Science, Technology and Research (A\*STAR)  
2 Fusionopolis Way, Innovis, #08-03, Singapore 138634

† Footnotes relating to the title and/or authors should appear here.  
Electronic Supplementary Information (ESI) available: [details of any supplementary information available should be included here]. See DOI: 10.1039/x0xx00000x

nanocubes. We first maximize the SERS performance by modulating both the ZIF thickness and interparticle spacing, and further highlight the importance of intense EM field to better utilize the sorbed molecules in 3D space for SERS detection. Subsequently, we demonstrate MOF layer is critical for in situ kinetics investigations due to their excellent sensitivity and responsiveness towards gas detection compared to their absence. Exploiting the molecular vibrational fingerprint, our plasmonic nose is also able to “sniff out” and quantify several toxic VOCs and PAHs vapors (such as toluene, 4-methylbenzenethiol (4MBT), 2-naphthalenethiol (2NT) and chloroform) below regulatory limits, surpassing the human nose. Together with its excellent recyclability, these valuable insights are important to push for even better regulatory standards to enforce safety and conserve life.

We design ultrasensitive Ag@ZIF-based plasmonic nose (Figure 1A) by leveraging on both ZIF's preconcentration effect for gas accumulation, and concentrating plasmon-induced EM fields via organization of Ag nanocubes (Figure S1, S2). Using a repeated growth method, we encapsulate the assembled Ag nanocubes array on Si substrate with ZIF film via immersion into a solution containing zinc nitrate and 2-methylimidazole.<sup>4</sup> ZIF first nucleates onto the Ag nanocubes and silicon surface, and then thickens into a polycrystalline thin film over the array (Figure S3, S4). By increasing growth cycles (from 1 to 5), the thickness of the pristine ZIF film above the nanocubes (Figure 1A) can be systematically controlled from 8 to 287 nm (Figure 1B, 1C, S3). The ZIF film also becomes more continuous and homogenous as its coverage on the Ag nanocubes array increases from an initial 64% to an eventual 100% (Figure S5). Henceforth, various Ag@ZIF platforms are described as 'Ag@ZIF-(X)', where X denotes the ZIF growth cycles to form respective Ag@ZIF.

The thickness and coverage of ZIF film over Ag nanocube array directly impact the volume of gas that can be preconcentrated near the plasmonic nanoparticles surface for enhanced SERS detection. We investigate this by assessing the SERS responses of gas molecules recorded from Ag@ZIF platforms constructed from different ZIF growth cycles. We choose 4MBT as our probe because their distinct and consistent vibrational fingerprints allow representative comparison across various Ag@ZIF platforms. Prior to SERS measurement, Ag@ZIF platforms are thermally-activated and this treatment process does not affect Ag@ZIF's structural integrity (Figure 1D, S6). 4MBT solid is then incubated in an enclosed Raman cell with various platforms to allow vaporization of 4MBT into an equilibrium state in the closed system (Figure 1F). All Ag@ZIF platforms exhibit the characteristic peaks of 4MBT at  $1079\text{ cm}^{-1}$  ( $\nu_{\text{CS}}$ ,  $\beta_{\text{CCC}}$ ),  $1181\text{ cm}^{-1}$  ( $\nu_{\text{C=C}}$ ) and  $1595\text{ cm}^{-1}$  ( $\nu_{\text{C=C}}$ ) (Figure 1E).<sup>8</sup> Using the most intense band at  $1079\text{ cm}^{-1}$ , we observe a general increase in SERS intensity with thicker ZIF film. This is followed by the plateau of SERS intensity at  $(620 \pm 84)$  counts beyond the third cycle ( $d = 146\text{ nm}$ ) (Figure 1G). Consequently, the optimal ZIF thickness is determined at  $146\text{ nm}$ , which demonstrates a notable  $\sim 2.5$ -fold higher SERS activity compared to control Ag nanocube array without ZIF. This corresponds to an analytical

enhancement factor (AEF) of  $7.6 \times 10^6$  and  $3 \times 10^6$  for Ag@ZIF-(3) and control platform, respectively (Supporting Text 1).

The effect of ZIF growth cycles on Ag nanocubes highlights two contributing factors affecting SERS response – (1) an increase in film coverage and (2) in film thickness. While the increment in film coverage does increase the averaged SERS intensity, we note the sudden surge in SERS activity enabled by thicker ZIF film in Ag@ZIF-(3). This is due to the increased accumulation of gas along the z-depth (Figure 1F, S5) which maximizes the amount of analyte molecules within the intense and z-extended EM hot spots imparted by Ag nanocubes. Beyond the optimal thickness ( $3^{\text{rd}}$  cycle), the SERS intensity remains constant because any further accumulation of 4MBT along the z-direction is too far to experience the enhanced EM field and therefore, contributes negligibly to the overall SERS responses. Our Ag@ZIF ensemble is a clear progress from previous MOF-SERS works involving core-shell Ag@ZIF, where the latter demonstrates an optimal shell thickness of only  $3.2\text{ nm}$  using small ( $\sim 54\text{ nm}$ ) and pseudo-spherical nanoparticles.<sup>9</sup> The better utilization of the sorbed gas molecules could potentially arise from the more intense EM field enhancements. This is achieved using larger and shape-controlled Ag nanocubes and the extensive plasmonic coupling among adjacent particles.

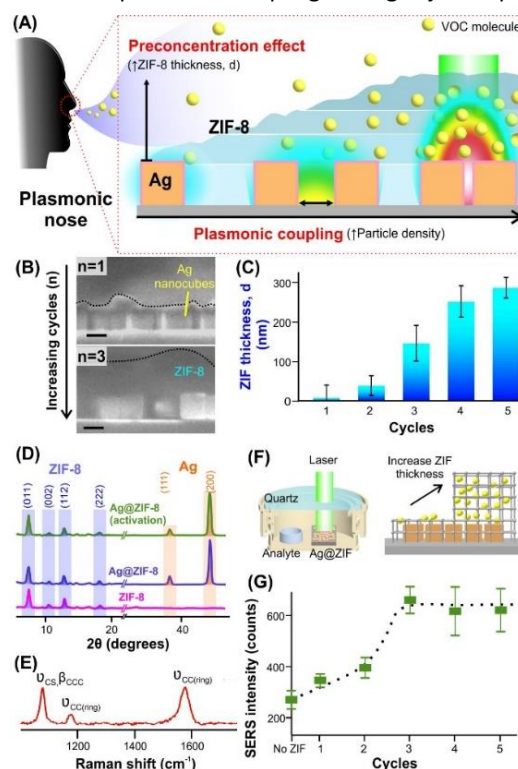


**Figure 1.** (A) Scheme of “plasmonic nose” concept based on a two-pronged approach in tuning plasmonic hotspots and MOF thickness. (B) Cross-sectional SEM images of the ZIF film thickness after one (top) and three (bottom) ZIF growth cycles. Scalebar, 100 nm. (C) Thickness of ZIF film above the nanocubes as a function of growth cycles. (D) XRD characterization of Ag@ZIF before (blue) and after activation at  $120\text{ }^{\circ}\text{C}$  for 2 hours under vacuum (green), and also neat ZIF film (pink). (E) SERS spectrum of 4-methylbenzenethiol (4MBT) recorded from Ag@ZIF-(3). (F) Schemes depicting the SERS experimental set-up (left) and increased accumulation of gas with increasing thickness of ZIF film (right). (G) SERS intensity of 4MBT vapor as a function of ZIF growth cycles. The SERS intensities are based on 4MBT's characteristic vibrational mode at  $1079\text{ cm}^{-1}$ . Eye-guided dotted line represents the trend.

Notably, these observations are also aligned with previous theoretical studies reporting that smaller nanoparticles are inherently weaker scatterer and experience faster electric field decay<sup>10</sup> because of surface plasmon damping via non-radiative processes.<sup>11, 12</sup> Hereon, we use Ag@ZIF-(3) for optimization of SERS performance.

Plasmonic coupling modulation between Ag nanocubes is also key to effect intense EM field enhancements in 3D space and can be achieved by controlling the interparticle spacing (Figure 2A).<sup>13</sup> Briefly, we use Langmuir-Blodgett as a liquid-air interfacial assembly technique to systematically vary the Ag nanocube packing density.<sup>14, 15</sup> Our platform does not involve polymeric template, therefore eliminating potential background signal interferences.<sup>16</sup> Uniform and large-scale array comprising of a monolayer of Ag nanocubes with precisely tunable compactness is realized via the isothermal compression by a mechanical barrier to alter interfacial surface pressure ( $\Pi$ ). As  $\Pi$  is varied from 4 to 18 mN/m, the interfacial film evolves from light brown to metallic silver due to enhanced plasmonic coupling as its compactness increases from a particle density of 9 to 51 particles/ $\mu\text{m}^2$ , respectively (Figure 2B, 2C, S7).<sup>17</sup> Using Ag@ZIF-(3) platform and 4MBT as gaseous probe, we observe an obvious ~5-fold linear enhancement to SERS sensitivity as  $\Pi$  increases from 4 to 16 mN/m owing to enhanced plasmonic coupling between adjacent particles (Figure 2D). Constant SERS intensity at 617 counts with negligible improvements are obtained for  $\Pi = 18$  mN/m. This is possibly due to the balance between stronger plasmonic coupling with opposing effect arising from reduced molecular accessibility to the plasmonic surfaces at high particle compactness.<sup>18</sup> It is also noteworthy that Ag@ZIF-(3) fabricated at a more compact  $\Pi = 16$  mN/m enables a homogenous distribution of SERS activities across the entire platform while control substrate formed at  $\Pi = 4$  mN/m are sporadically located (Figure 2B, 2C). Collectively, our findings clearly demonstrate that both the MOF thickness and the intense EM field rendered by extensive plasmonic coupling within a compact Ag nanocube array are the keys to maximize SERS sensitivity crucial for ultrasensitive gas phase detection.

We further demonstrate the concept of the plasmonic nose to capture and direct gaseous analytes towards the ZIF-encapsulated plasmonic surface for rapid molecular detection. Time-dependent SERS monitoring on the sorption of vapor 4MBT is employed to reveal the sorption kinetics of gas to Ag surface in both Ag@ZIF-(3) and control Ag nanocube without ZIF coating (Figure 2E). For Ag@ZIF-(3) platforms, 4MBT's SERS intensity increases exponentially from  $(40 \pm 10)$  to  $(432 \pm 5)$  counts within 80 seconds and subsequently plateaus after equilibrium is reached (Figure 2F, S8). More importantly, the additional ZIF film over the Ag nanocubes improves SERS performance by > 3-fold over the control, where the latter acquires a lower intensity of  $(136 \pm 3)$  counts only after 120 s. Using a Lagergren pseudo first order sorption kinetics, we further determine that the sorption rate constant of Ag@ZIF-(3) is  $66 \text{ ms}^{-1}$  and notably  $\geq 2$ -fold higher than the control. This evidently underlines that Ag@ZIF platform is critical to impart intense and rapid SERS response (Figure 2F, 2G), whereby ZIF swiftly captures and concentrates analytes to the plasmonic

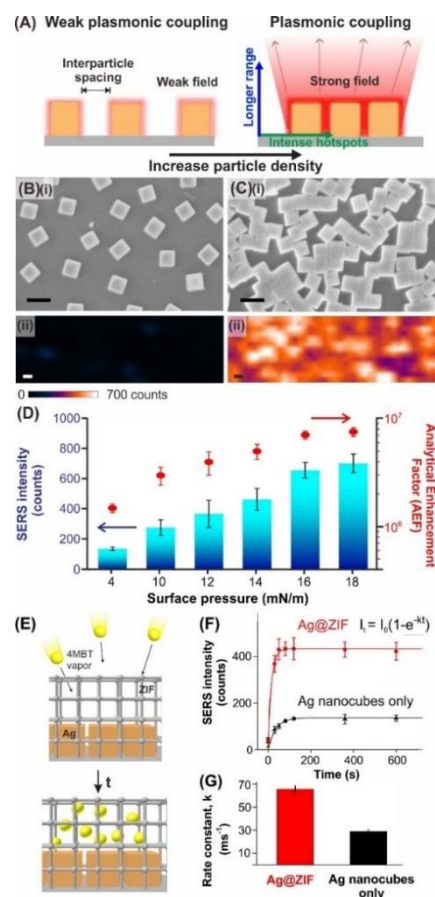


**Figure 2.** (A) Scheme shows reducing the interparticle spacing enhances the plasmonic coupling and the resultant EM field surrounding the Ag nanocubes. (B, C)(i) SEM images and (ii) SERS image of Ag nanocube array prepared at surface pressures of 4 and 16 mN/m. Scale bar of SEM, 200 nm. Scale bar of SERS image, 1  $\mu\text{m}$ . (D) Comparison of SERS intensity and respective AEF using Ag@ZIF-(3) arrays prepared at various surface pressures. (E) Scheme depicting temporal gas sorption. (F) Time-dependent SERS comparing platforms with (red) and without (black) ZIF film upon incubation of 4MBT vapor. (G) Graph depicting the rate constants of respective platforms. Intensities are based on 4MBT characteristic SERS band at  $1079 \text{ cm}^{-1}$ .

surface while the intense EM hot spots conferred by Ag nanocube array permits sensitive monitoring of temporal sorption events.

Using our optimized Ag@ZIF-(3) ensemble fabricated at  $\Pi = 16$  mN/m (hereon termed as Ag@ZIF plasmonic nose), we demonstrate the quantitative and molecular-level identification of VOCs, which are toxic yet prevalent in air due to their wide industrial usage (Figure 3A). We first use commonly-used toluene as our model VOC because it has no chemical affinity to Ag. This enables us to examine our platform as a universal gas sensor for a wide range of toxic VOC and polycyclic aromatic hydrocarbon (PAHs). SERS responses recorded from our Ag@ZIF plasmonic nose clearly exhibit vibrational features unique to toluene even at a remarkable detection limit down to 200 ppm ( $\text{AEF} > 2 \times 10^5$ ), with distinctive peaks at  $1002 \text{ cm}^{-1}$ ,  $1030 \text{ cm}^{-1}$ , and  $1210 \text{ cm}^{-1}$  indexed to  $\nu_{\text{C-H}}$ .<sup>19</sup> Ag@ZIF also permits the linear quantification of toluene vapor over three orders of magnitude (200 to 20000 ppm) (Figure 3B). Quantifying toluene concentration in this range is crucial as the hazardous vapor could lead to acute symptoms ranging from throat/eye irritation to even death. The detection limit is also well within OSHA



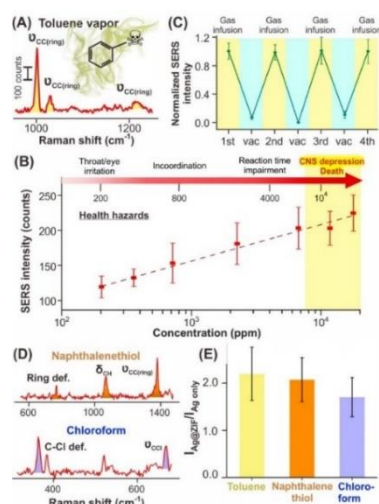


**Figure 3.** (A) SERS spectrum of toluene vapor recorded using Ag@ZIF (B) Linear correlation of SERS intensities with toluene concentration. Dotted line represents the linear regression line. The potential acute health hazards are included. (C) Normalized SERS intensities measured from a single Ag@ZIF platform after exposure to toluene and vacuum repeatedly. The recyclability is reflected by the absence of toluene spectra after vacuum and consistent signals upon toluene incubation. The intensities are based on the band at  $1002\text{ cm}^{-1}$ . (D) SERS spectra for 2NT (top) and chloroform (bottom) vapor. (E) Enhanced detection of toluene, 2NT, and chloroform of Ag@ZIF platforms when compared to control Ag nanocube array in the absence of ZIF.

exposure limit which is vital to drive continual revision of toxic gas threshold for better industrial safety. Our plasmonic nose is also recyclable owing to their reversible host-guest interactions upon subjecting to vacuum, as shown from the reproducible SERS readout ( $< 1\%$  standard deviation) and similar structural integrity after 4 cycles of detection (Figure 3C, S9).

Our Ag@ZIF plasmonic nose is also versatile and can discern a series of PAH and VOC including chloroform and 2NT, which are frequently emitted by the industry/laboratories and require constant monitoring. Both analyte exhibit their unique SERS vibrational features even at respective detection limits. For chloroform, the peaks at  $363\text{ cm}^{-1}$  and  $665\text{ cm}^{-1}$  correspond to the  $\delta_{\text{C-Cl}}$  and  $\nu_{\text{C-Cl}}$  respectively, while 2NT is identified by the peaks at  $780\text{ cm}^{-1}$  ( $\delta_{\text{C=C}}$ ),  $1065\text{ cm}^{-1}$  ( $\delta_{\text{CH}}$ ) and  $1375\text{ cm}^{-1}$  ( $\nu_{\text{C=C}}$ ) (Figure 3D, S10).<sup>20, 21</sup> Notably, the LOD of 2NT is down to the 50 ppb, 15-fold lower than the exposure limits of  $5\text{ mg/m}^3$  ( $0.7\text{ ppm}$ ). The ability to distinguish different gas molecules via their vibrational signatures is vital to accurately attribute the gas and eliminate false positives – a function lacking in most commercial detectors. Importantly, our platform directly measures gas species from air which surpasses previous SERS-based gas detectors that typically requires post-treatment of gas.<sup>22</sup> We also note the consistent  $\sim 2$ -fold enhancement to SERS intensity across all vapor analytes when compared to control platform without ZIF, further affirming the preconcentration effect imparted intrinsically by the ZIF film (Figure 3E, S10). Further comparison of SERS performance across other control platforms such as bare Ag nanocubes, core-shell Ag@ZIF, Ag film@ZIF and ZIF only platforms highlights the importance of each individual components in our combinative approach (Figure S11, S12). Our ensemble clearly outperforms all other platforms, emphasizing the need to concentrate both molecules and EM field.

In conclusion, we have designed a MOF-encapsulated Ag nanocubes-based plasmonic nose capable of ultrasensitive SERS recognition of multiple gaseous VOCs down to ppm levels. Two key factors are essential towards the realization of efficient plasmonic nose: (1) the thickness of the pristine ZIF film which directly influences the preconcentration of molecules in the z-depth, and (2) extensive plasmonic coupling arising from compact Ag nanocube array that allows 5-fold amplification in SERS signal. Notably, our plasmonic nose enables both in situ gas sorption kinetics analysis, and quantitative detection of non-adsorbing toluene vapor. Our plasmonic nose is also versatile and can discern a series of toxic VOCs at the molecular-level. These valuable insights could potentially provide a paradigm shift in the future design of MOF-SERS sensors, empowering ultrasensitive detection capability beyond boundaries which is critical in the shaping of better toxic gas regulation for industrial safety.

## Notes and references

1. L. Mølhave, B. Bach and O. F. Pedersen, *Environ. Int.*, 1986, **12**, 167-175.
2. S. Nie and S. R. Emory, *Science*, 1997, **275**, 1102.
3. X. Liu, S. Cheng, H. Liu, S. Hu, D. Zhang and H. Ning, *Sensors (Basel, Switzerland)*, 2012, **12**, 9635-9665.
4. G. Lu and J. T. Hupp, *J. Am. Chem. Soc.*, 2010, **132**, 7832-7833.
5. W. Vandezande, K. P. F. Janssen, F. Delport, R. Ameloot, D. E. De Vos, J. Lammertyn and M. B. J. Roeffaers, *Anal Chem*, 2017, **89**, 4480-4487.
6. Y. Hu, J. Liao, D. Wang and G. Li, *Anal Chem*, 2014, **86**, 3955-3963.
7. G. Zheng, S. de Marchi, V. López-Puente, K. Sentosun, L. Polavarapu, I. Pérez-Juste, E. H. Hill, S. Bals, L. M. Liz-Marzán, I. Pastoriza-Santos and J. Pérez-Juste, *Small*, 2016, **12**, 3935-3943.
8. D. L. Jeanmaire and R. P. Van Duyne, *J. Electroanal. Chem. Interfacial. Electrochem.*, 1977, **84**, 1-20.
9. L. He, Y. Liu, J. Liu, Y. Xiong, J. Zheng, Y. Liu and Z. Tang, *Angew. Chem. Int. Ed.*, 2013, **52**, 3741-3745.
10. G. Kumari, J. Kandula and C. Narayana, *J. Phys. Chem. C*, 2015, **119**, 20057-20064.
11. K. Kolwas and A. Derkachova, *Opto-Electron. Rev.*, 2010, **18**, 429-437.
12. K. G. Stamplecoskie, J. C. Scaiano, V. S. Tiwari and H. Anis, *J. Phys. Chem. C*, 2011, **115**, 1403-1409.
13. L. Guerrini, F. McKenzie, A. W. Wark, K. Faulds and D. Graham, *Chem. Sci*, 2012, **3**, 2262-2269.
14. A. Tao, F. Kim, C. Hess, J. Goldberger, R. He, Y. Sun, Y. Xia and P. Yang, *Nano Lett.*, 2003, **3**, 1229-1233.
15. Y. Yang, Y. H. Lee, I. Y. Phang, R. Jiang, H. Y. F. Sim, J. Wang and X. Y. Ling, *Nano Lett.*, 2016, **16**, 3872-3878.
16. L. E. Kreno, N. G. Greeneltch, O. K. Farha, J. T. Hupp and R. P. Van Duyne, *Analyst*, 2014, **139**, 4073-4080.
17. H. K. Lee, Y. H. Lee, Q. Zhang, I. Y. Phang, J. M. Tan, Y. Cui and X. Y. Ling, *ACS applied materials & interfaces*, 2013, **5**, 11409-11418.
18. D. A. Genov, A. K. Sarychev, V. M. Shalaev and A. Wei, *Nano Lett.*, 2004, **4**, 153-158.
19. K. S. Pitzer and D. W. Scott, *J. Am. Chem. Soc.*, 1943, **65**, 803-829.
20. R. A. Alvarez-Puebla, D. S. Dos Santos Junior and R. F. Aroca, *Analyst*, 2004, **129**, 1251-1256.
21. T. Shimanouchi, *National Bureau of Standards*, 1972, 1-160.
22. P. A. Mosier-Boss and S. H. Lieberman, *Anal Chim Acta*, 2003, **488**, 15-23.

## Experimental Procedures

**Chemicals.** Silver nitrate ( $\geq 99\%$ ), anhydrous 1, 5-pentanediol ( $\geq 97\%$ ), poly (vinylpyrrolidone) (PVP; average MW = 55000), 1H,1H,2H,2H-perfluorodecanethiol (PFDT,  $\geq 97\%$ ), zinc nitrate hexahydrate (98%), 2-methylimidazole (99%), 4-methylbenzenethiol (4MBT,  $\geq 98\%$ ), 2-naphthalenethiol (99%), chloroform, toluene, decane (anhydrous,  $\geq 99\%$ ), were purchased from Sigma Aldrich; copper (II) chloride ( $\geq 98\%$ ) was from Alfa Assar; ethanol (ACS, ISO, Reag. Ph. Eur) was from EMSURE®. All chemicals were used without further purification. Milli-Q water ( $> 18.0\text{ M}\Omega\cdot\text{cm}$ ) was purified with a Sartorius Arium® 611 UV ultrapure water system.

**Synthesis and purification of Ag nanocubes.** Ag nanocubes were synthesized in high yield via the polyol method according to literature.<sup>[1]</sup> Copper (II) chloride (8 mg/mL), poly (vinylpyrrolidone) (20 mg/mL) and silver nitrate (20 mg/mL) were separately dissolved in 10 mL 1, 5-pentanediol after repeated sonication and vortex mixing. 35  $\mu\text{L}$  copper (II) chloride solution was subsequently added to the silver nitrate solution. 20 mL of 1,5-pentanediol was added into a 100-mL round bottomed flask and heated to 190 °C for 10 min. 250  $\mu\text{L}$  poly(vinylpyrrolidone) precursor was added to flask dropwise every 30 s while 500  $\mu\text{L}$  silver nitrate precursor was injected every minute using a quick addition. The addition process continued until the greenish coloration of the mixture faded off.

For the purification of Ag nanocubes, 1, 5-pentanediol was first removed from the mixture through centrifugation and then washed with ethanol. The Ag nanocubes were then dispersed in 10 mL ethanol and 100 mL aqueous poly (vinylpyrrolidone) solution (0.2 g/L). The resulting solution was vacuum filtered using Durapore® polyvinylidene fluoride filter membranes (Millipore) with pore sizes ranging from 5000, 650, 450, and 220 nm, repeated several times for each pore size. The Ag nanocubes were then re-dispersed in ethanol (10 mg/mL) and stored in fridge for further use.

**Assembly of Ag nanocubes via Langmiur-blodgett method.** Si (100) substrates were cleaned prior to assembly of Ag nanocubes using oxygen plasma (FEMTO SCIENCE, CUTE-MP/R, 100 W) for 5 min. The surface pressure was zeroed before addition of PVP-caped Ag nanocubes. 700  $\mu\text{L}$  of the ethanolic purified Ag nanocubes was dispersed in 1050  $\mu\text{L}$  of chloroform and then added carefully to the surface of the water in the Langmiur-Bblodgett trough (KSV NIMA, KN1002). The surface pressure can be tuned by moving the mechanical barrier of the machine. Surface pressure of 4, 8, 10, 12, 14, 16, 18 mN/ m were performed, and the pull rates and compression rate were fixed at 2 mm/ s.

**1H,1H,2H,2H-perfluorodecanethiol (PFDT) functionalization of Ag nanocubes.** The removal of surfactant from Ag nanocubes surface was done by functionalizing the assembled Ag nanocubes with PFDT. The assembled Ag nanocube array was immersed in 5 mM of PFDT methanolic solution for at least 15 hours.

**Growth of ZIF-8 film on PFDT-capped Ag nanocubes array.** ZIF-8 film was grown on the nanocubes array using a procedure reported from literature.<sup>[2]</sup> 2 ml of methanolic  $\text{Zn}(\text{NO}_3)_2$  (25 mM) was added to 2 ml of methanolic 2-methylimidazole (mIM; 50 mM) and mixed quickly for 5 s. For one growth cycle, the PFDT-capped Ag nanocubes substrate was immersed in the solution for 40 minutes, and then washed with copious amount of methanol and dried with nitrogen gas several times to remove excess ZIF-8 crystals. The procedure was repeated (1 – 5 times) using fresh  $\text{Zn}(\text{NO}_3)_2$  and 2-methylimidazole solutions to obtain ZIF-8 films of increasing thickness.

**Activation of Ag@ZIF substrate.** The Ag@ZIF substrates were thermally activated to remove any solvent molecules within its pores by heating the substrate under vacuum at 120°C for 2 hours. The substrates are used immediately after activation.

**Fabrication of Ag film@ZIF.** 25-nm Ag film was deposited onto the  $\text{O}_2$  plasma-treated Si wafer using a thermal evaporator deposition system from Syskey Technology Corporation (Taiwan) system. The deposition rate was 0.5 Å/s which was monitored using a quartz crystal microbalance. Ag target with 99.99% purity was purchased from Zhongnuo Advanced Material (Beijing) Technology co., Ltd. The Ag film was then functionalized with PFDT and then with 3 layers of ZIF-8 using the same procedures as above.

**Fabrication of ZIF only.** Silicon substrate was directly immersed in a fresh mixture containing 2 ml of methanolic  $\text{Zn}(\text{NO}_3)_2$  (25 mM) and 2 ml of methanolic 2-methylimidazole (mIM; 50 mM) for 40 minutes, and then washed and dried under nitrogen flow. Additional 2 growth cycles were carried out to achieve ZIF film of similar thickness to Ag@ZIF platform.

**Synthesis of Ag@ZIF core-shell.** 250  $\mu\text{L}$  of  $\text{Zn}(\text{NO}_3)_2$  (25 mM) was added to a vial of 1.3 mL methanol and stirred at 500 rpm for 5 minutes. 250  $\mu\text{L}$  of methanolic 2-methylimidazole (50 mM) was then added, followed by the immediate addition of 200  $\mu\text{L}$  Ag nanocubes solution (4.7 mg/mL). The mixture was stirred for another 90 minutes at 500 rpm. Excess reagents were removed by centrifugation and the core-shell nanoparticles were then washed twice with methanol and then finally re-dispersed in methanol.

**SERS measurement of VOCs and PAH vapors.** The activated Ag@ZIF substrate or Ag nanocubes only substrate is incubated together with 200  $\mu\text{L}$  or 0.05 g of solvent/solid at ambient conditions in an enclosed Raman cell printed using Form 1+ stereolithography 3D printer. The SERS detection was performed 10 or 30 mins after incubation of vapor at room temperature ( $\sim 20^\circ\text{C}$ ). Time-dependent investigations were performed using Ag@ZIF-(3) fabricated at  $\Pi = 12 \text{ mN/m}$ . For VOCs detection, optimized Ag@ZIF-(3) fabricated at  $\Pi = 16 \text{ mN/m}$  is employed. SERS measurement is performed

using a hyperspectral x-y imaging mode with an acquisition time of 1 s/line or 15 s/line (for toluene and chloroform) and a laser power of 0.5 mW or 0.38 mW respectively, unless otherwise stated.

**Characterization.** Scanning electron microscope (SEM) and energy-dispersive X-ray spectroscopy (EDS) imaging was performed using JEOL-JSM-7600F microscope. UV-vis spectra were measured with Cary 60 UV-vis spectrometer. Substrate X-ray diffraction patterns were recorded on a Bruker GADDS XRD diffractometer with Cu K $\alpha$  radiation. SERS measurements were performed using x-y hyperspectral imaging mode of the Ramantouch microspectrometer (Nanophoton Inc., Osaka, Japan) with an excitation wavelength of 532 nm and laser power of 0.5 mW or 0.38 mW. A 50 $\times$  objective lens (N.A. = 0.55) with 1 s or 15 s acquisition time was used for data collection. All SERS spectra were obtained by averaging the individual SERS spectra within the SERS image.



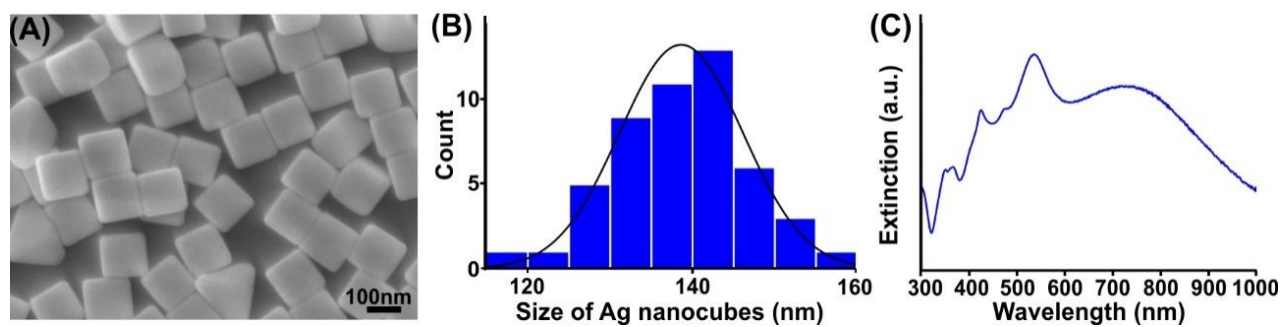


**Figure S1.** Characterization of as-synthesized PVP-coated Ag nanocubes. (A) SEM image of Ag nanocubes. (B) Size distribution of Ag nanocube edge length. The average edge length is measured at  $(138 \pm 7)$  nm. (C) UV-vis extinction spectra of the PVP-coated Ag nanocubes colloidal solution in ethanol. The peaks at 353, 400, 505 and 724 nm that can be assigned to octupole (353 nm), quadrupole (400 nm and 505 nm), and dipole resonances (724 nm).<sup>[3]</sup>

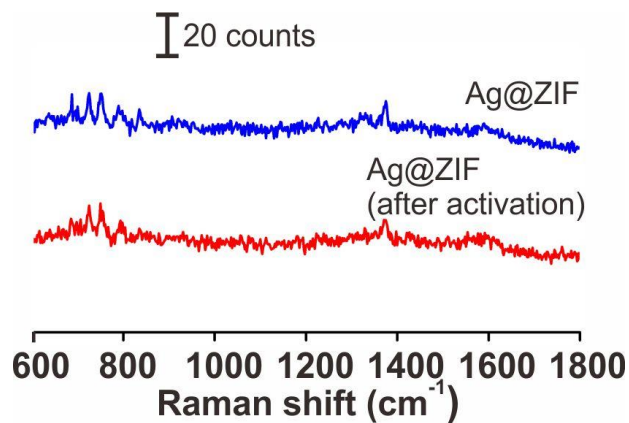


**Figure S2.** Background spectra of Ag@ZIF platform before (blue) and after (red) thermal activation. The clean background arises due to the functionalization of PFDT ligands onto the Ag nanocubes surface, while the similar vibrational signatures reflect the chemical stability of the platform even after thermal activation.

ZIF provides chemically- and thermally-stable nanoporosity required to preconcentrate various vapor molecules near the Ag surface, while perfluorodecanethiol (PFDT)-capped Ag nanocube offers strong SERS activity with clean signal background for accurate molecular identification.<sup>[4]</sup>

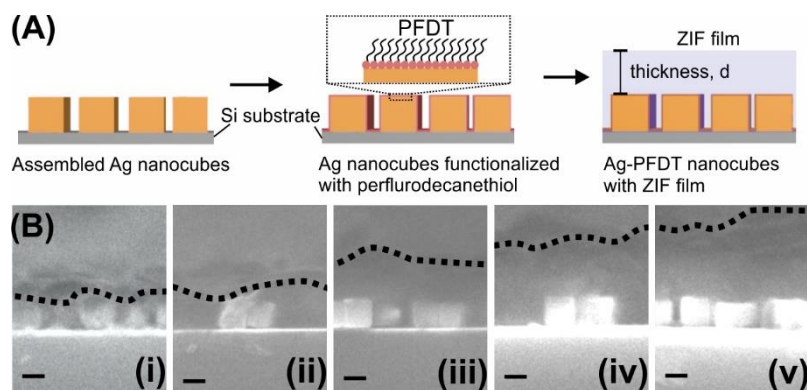


**Figure S3.** (A) Scheme of thin film formation of ZIF-8 onto assembled Ag nanocubes substrate; Ag nanocubes array are first immersed into PFDT solution (5 mM) for above 15 hours before being immersed into a mixture of freshly prepared  $\text{Zn}(\text{NO}_3)_2$  (25 mM) and 2-methylimidazole (50 mM) for 40 minutes. (B)(i – v) Cross sectional scanning electron microscopy (SEM) images of the ZIF-8 film thickness after 1 – 5 ZIF-8 growth cycles. Scale bar, 100 nm.

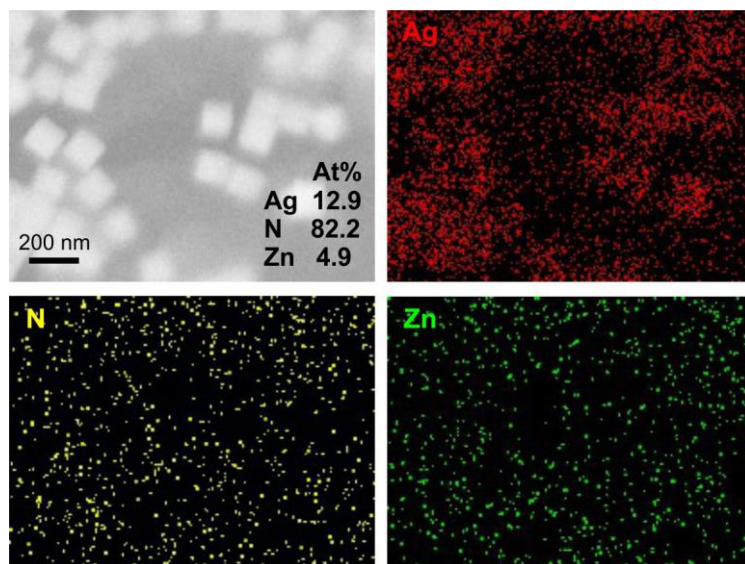


**Figure S4.** EDS elemental mapping of Ag@ZIF substrate indicating the elemental distribution of Ag (red), N (yellow) and Zn (green).

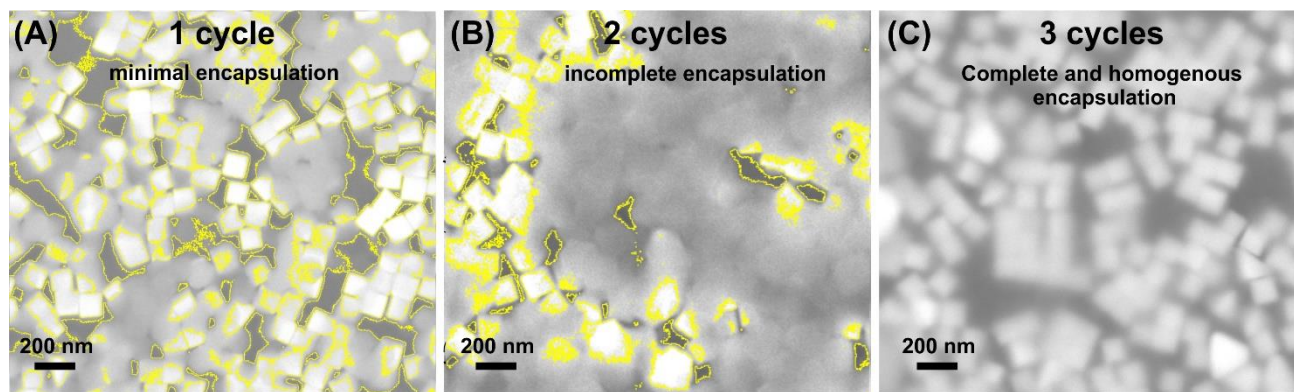


**Figure S5.** (A-C) SEM images of ZIF-8 film growth after 1 - 3 cycles. Dotted lines show the ZIF-8 film growth over the nanocubes. The first cycle result in minimal film growth and individual ZIF-8 crystals are observed. Upon additional growth cycle, the film thickens and becomes more continuous but is insufficient to completely encapsulate the Ag nanocubes array. A minimum of 3 cycles is needed to allow complete and homogenous encapsulation of the nanocubes. Yellow lines outline the ZIF-8 film overgrowth on the Ag array.

As the growth cycle is increased from 2 to 3, the coverage increases by 36% to allow complete encapsulation. This enables more gas analyte to accumulate at the nanoparticle surface, which consequently leads to an increase in SERS signal. However, extrapolating from the previous trend of Ag@ZIF-1 to Ag@ZIF-2, this increase in encapsulation is expected to result in linear increase of SERS activity, instead of the sharp and drastic increase in SERS intensity achieved by the Ag@ZIF-3. This therefore evidently demonstrates that the amplified signal of the Ag@ZIF-3 platform is attributed to both the increase in coverage and thickness of the ZIF-8 film, where more gas analyte is allowed to accumulate in the x-, y-, and z- direction respectively.

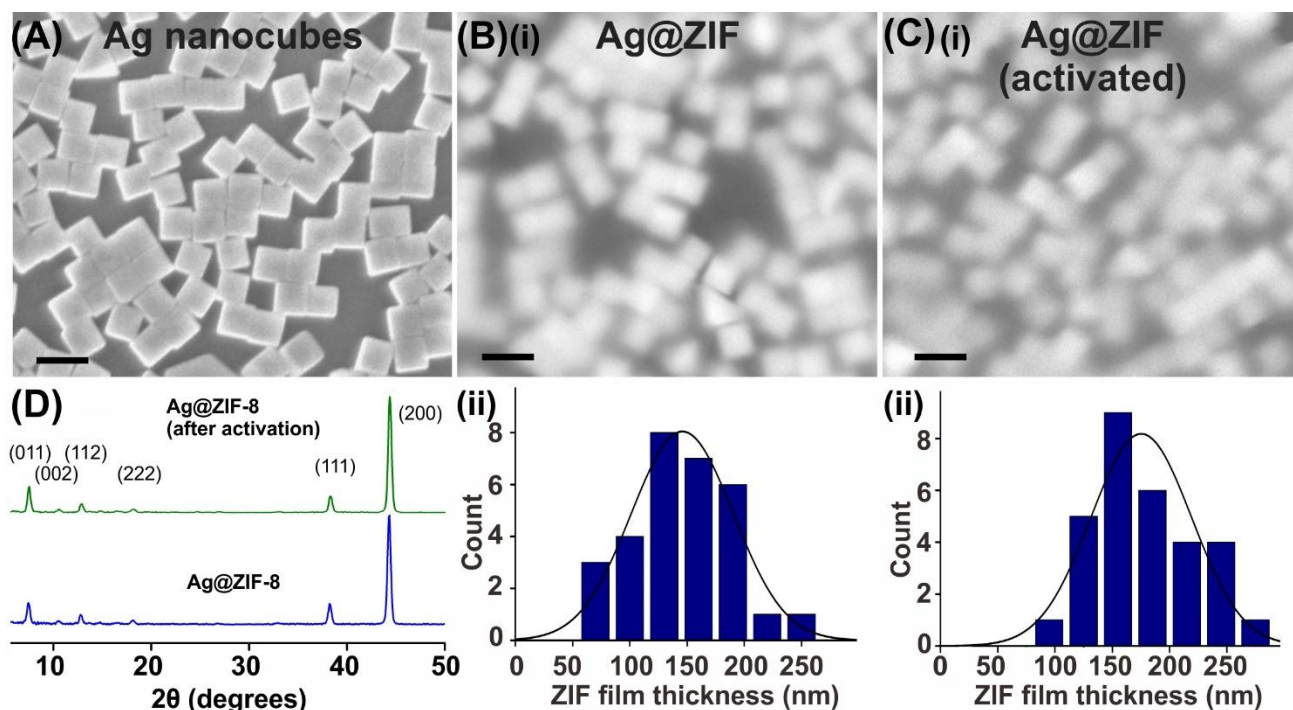


**Figure S6.** SEM images of Ag nanocubes assembled using surface pressure of 16 mN/ m after (A) functionalization with PFDT, followed by (B) (i) 3 cycles of ZIF-8 and then (C) (i) thermally activated under vacuum at 120°C for 2 hours. Scale bar, 200 nm. (ii) Thickness distribution of the ZIF film. Thermal stability of ZIF-8 film over Ag nanocubes is reflected by the minimal changes even after activation. (D) XRD spectra before and after activation shows minimal difference.

Ag@ZIF platforms are thermally-activated prior to SERS measurement and this treatment process does not affect Ag@ZIF's structural integrity, as reflected by their similar XRD patterns, film morphology and SERS spectra before and after thermal activation.



### Supporting Text S1: Calculation of Analytical Enhancement Factor (AEF)

Calculation of AEF using saturated methylbenzenethiol gas is as follows:

$$\text{Analytical EF} = [I_{\text{SERS}} / I_{\text{Raman}}] \times [C_{\text{Raman}} / C_{\text{SERS}}]$$

where  $C_{\text{SERS}}$  and  $C_{\text{Raman}}$  are the corresponding concentration measured using Ag@ZIF substrate and normal Raman respectively.  $I_{\text{SERS}}$  and  $I_{\text{Raman}}$  are the signals recorded using SERS and normal Raman at their respective concentration per unit time.

$C_{\text{SERS}}$  is calculated by manipulating the terms in the ideal gas law:

$$C_{\text{SERS}} = \frac{n}{V} = \frac{p}{RT} = \frac{108}{8.31 * 298} = 0.0434 \text{ mol/m}^3$$

Where  $p$  is the partial pressure (= 108 Pa) at ambient temperature ( $T = 298 \text{ K}$ ), and  $R$  is the universal gas constant, 8.31 J/Kmol.

$C_{\text{Raman}}$  is calculated by dividing the density of 4MBT by its molecular weight:

$$C_{\text{Raman}} = \frac{\rho}{\text{MW}} = \frac{1.022 \text{ g/ml}}{124 \text{ g/mol}} = 0.008228 \text{ mol/ml}$$

Hence, using Ag@ZIF substrate formed using surface pressure of 16 mN/ m as an example,

$$\text{AEF} = [I_{\text{SERS}} / I_{\text{Raman}}] \times [C_{\text{Raman}} / C_{\text{SERS}}] = (660/ 18) \times (8228/ 0.0434)$$

$$= 7.10 \times 10^6$$

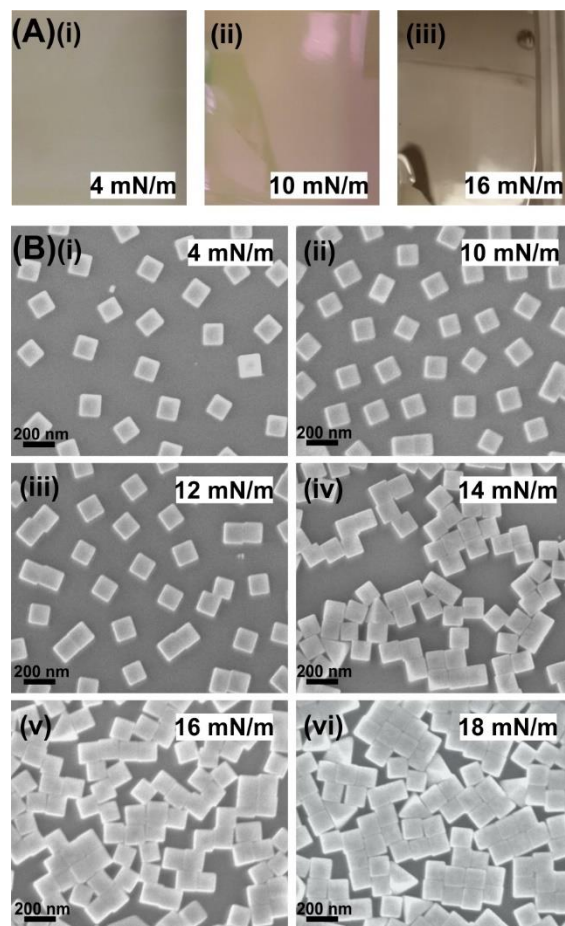


**Figure S7.** (A) (i-iii) Digital images of the visual changes observed as the compactness of the Ag nanocube array increases from 4, 10, 16 mN/m. (B) (i-vi) SEM images of assembled Ag nanocube array when surface pressure is 4, 10, 12, 14, 16, 18 mN/m respectively.

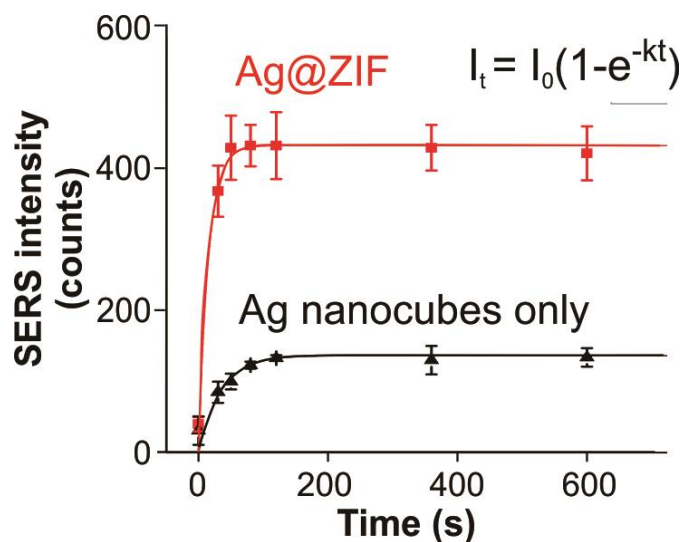


**Figure S8.** Time-dependent SERS measurement of 4-MBT sorption comparing platforms with (red) and without (black) ZIF film.

Both intensity-time curves can be fitted using a Lagergren pseudo first order adsorption kinetics<sup>[5]</sup> based on linear driving force model, which is inclined to physisorption of the analyte and follows the equation:  $I = I_{\max}(1 - e^{-kt})$  where  $I$  is the time-dependent SERS intensity (in counts) at time  $t$ ,  $I_{\max}$  the final equilibrium intensity and  $k$  ( $s^{-1}$ ) gives the pseudo first-order adsorption rate constant. Notably, the rate constant ( $66 \text{ ms}^{-1}$ ) is two-fold higher than the control, and the sharp increase in intensity within the first 80 s, further reflects advantage of ZIF-8 in enabling faster capture and preconcentration of the analyte molecules.

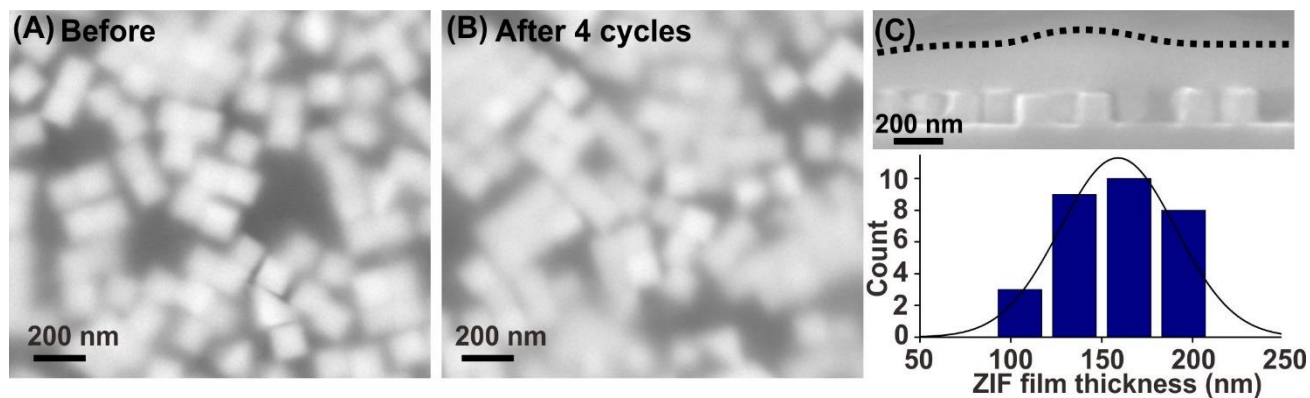


**Figure S9.** SEM images of Ag@ZIF substrate (A) before and (B) after exposure to toluene for four cycles. ZIF film remains intact even after subjecting the substrate to toluene vapor and vacuum repeatedly. (C) Cross-sectional SEM image (top) and corresponding ZIF-8 film thickness distribution of (B) (bottom). Dotted line denotes the ZIF film layer.

**Supporting Text S2: Calculation of vapor concentration from liquid reservoir**

The concentration of vapor toluene is varied from 200 to 20000 ppm in the incubation cell by changing the mole fraction of toluene in a toluene-decane mixture based on Raoult's law.<sup>[6]</sup>

Calculation of concentration of toluene vapor is as follows:

$$\text{Concentration (ppm)} = \frac{n_{\text{toluene}}}{n_{\text{total}}} \times 10^6$$

Where  $n_{\text{toluene}}$  and  $n_{\text{total}}$  is the number of moles of toluene and total number of gas molecules in the closed Raman cell respectively.

Using Raoult's law, which states that the partial pressure of a component in an ideal mixture is equals to the mole fraction of the component in the solution, the resultant partial vapor pressure of toluene in a toluene-decane mixture can be calculated. At temperature 298K, the vapor pressure of toluene and decane is 3760 Pa and 190 Pa respectively. By changing the mole ratio of decane/toluene, different concentration of toluene vapor can be obtained. The table below shows the volumes used for different vapor concentration.

Volume of Toluene (μl)	Volume of decane (μl)	Mole fraction of toluene	Partial Vapor Pressure of toluene (Pa)	Partial Vapor Pressure of decane (Pa)	Concentration of toluene (ppm)
1000	2000	0.47834	1799	99	17424
250	1000	0.31435	1182	131	11516
266	2235	0.17916	674	156	6594
35	1000	0.06031	227	179	2229
53	4950	0.01927	72	187	713
5	938	0.00968	36	189	358
3	1000	0.00547	21	190	203

For example, to achieve a vapor concentration of 17424 ppm, 1000 μl of toluene is mixed with 2000 μl of decane. Also given that the density of toluene and decane is 0.8669 g/ ml and 0.7300 g/ ml respectively,

$$\begin{aligned}\text{Mole fraction} &= \frac{V_1\rho_1/Mr_1}{V_1\rho_1/Mr_1 + V_2\rho_2/Mr_2} \\ &= \frac{0.1 \times 0.8669/92.14}{0.1 \times 0.8669/92.14 + 0.2 \times 0.73/142.29} = 0.47834\end{aligned}$$

Where V is the volume of component used in ml,  $\rho$  is the density in g/ml and Mr is the molecular weight in g/mol. Component 1 represents toluene while component 2 represents decane.

$$\text{Vapor pressure of toluene} = \text{mole fraction in solution} \times \text{vapor pressure}$$

$$= 0.47834 \times 3760 = 1799 \text{ Pa}$$

$$\text{Vapor Concentration (ppm)} = \frac{1799}{1799 + (1 - 0.47834) \times 190 + 101325} \times 10^6 = 17424$$

Reports have found that there is a risk of central nervous system (CNS) depression, the inhibition of brain activity, upon the first few minutes of toluene vapor exposure with concentration of 10000 – 30000 ppm, and possibly death for longer exposure times.<sup>[7]</sup> Even at lower concentrations, the acute effects include reaction time impairment and incoordination, and is especially dangerous for people working in high-hazard industries, thus emphasizing the necessity for rapid and timely detection of toluene leakages.



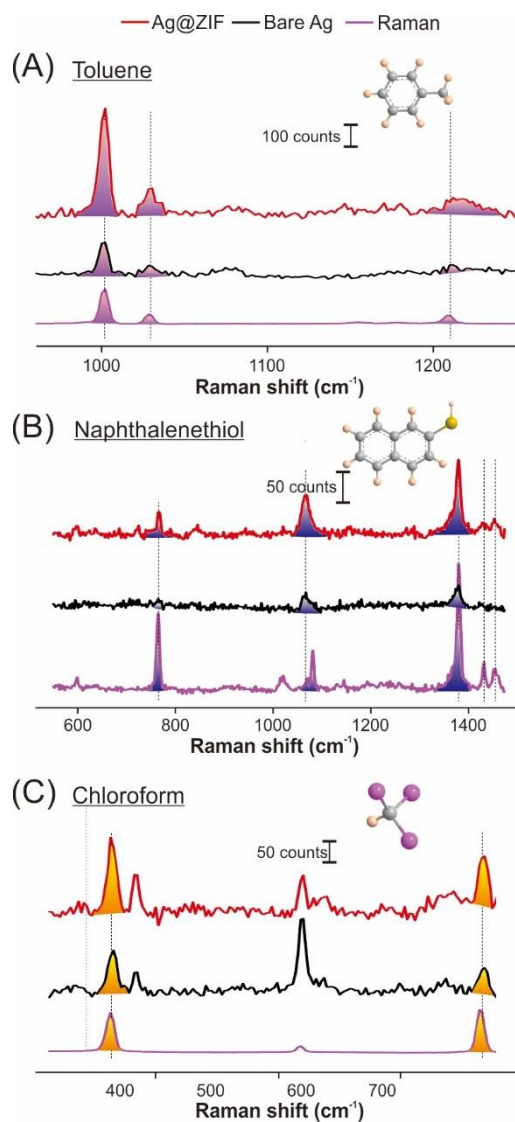


**Figure S10.** (A – C) SERS spectrum comparing detection of 2-naphthalenethiol, chloroform and toluene in gaseous phase using Ag@ZIF substrate (red) and Ag only (black). Raman spectra (pink) of the liquid solvent is added for reference. Inset shows the molecular structure of each VOC. Carbon, Hydrogen, Sulphur and Chlorine atoms are represented by grey, beige, yellow and magenta spheres respectively.

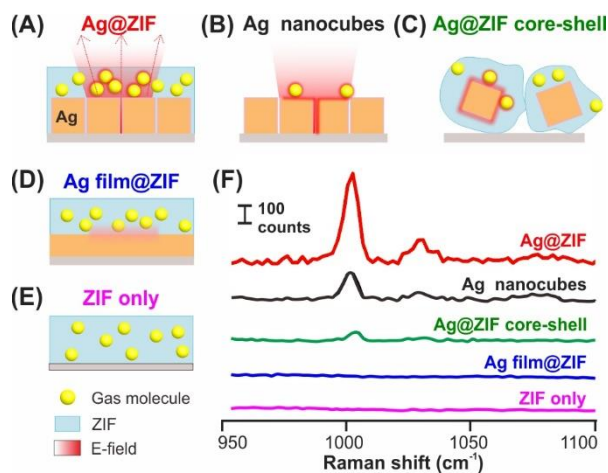


**Figure S11.** Demonstration on the superior SERS performance of Ag@ZIF. (A) Scheme of the Ag@ZIF platform with other control platforms such as (B) Ag nanocubes only, (C) Ag@ZIF core-shell particles, (D) Ag film@ZIF and (E) neat ZIF platform, and (F) comparison of their SERS activity.

We further compare the SERS performance of our Ag@ZIF plasmonic nose across other control platforms to highlight the importance of each individual components in our combinative approach. These control platforms include bare Ag nanocubes (absence of ZIF), core-shell Ag@ZIF dispersed onto a Si substrate (absence of intense plasmonic coupling), Ag film@ZIF and ZIF only platforms (Figure S11, S12). Generally, Ag@ZIF ensemble clearly outperforms all other platforms, achieving > 2-fold and 6-fold higher SERS sensitivity than Ag nanocubes only and Ag@ZIF core shell, respectively. The superior performance of our Ag@ZIF platform stems from its ability to concentrate both molecules and EM field cumulatively for better SERS enhancement compared to controls without ZIF or assembled arrays. We also note that control Ag film@ZIF and ZIF only platforms exhibit featureless spectra, again accentuating the need for high quality plasmonic crystal for sensitive SERS read-out. Our findings collectively highlight that MOF-enabled molecular preconcentration and intense EM field generated by extensive plasmonic coupling between Ag nanocubes are the key to ultrasensitive and swift vapor/gas detection. These benefits are highly sought after to ensure timely response necessary to protect the safety of the public in event of potential toxic gas leakage and/or air pollution from anthropogenic or natural sources.

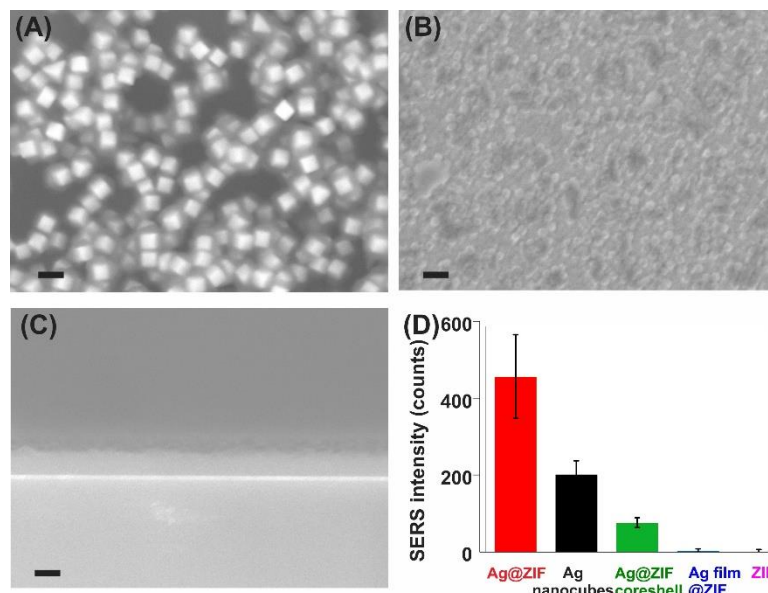


**Figure S12.** SEM images of the control platforms; (A) Ag@ZIF core-shell, (B) Ag film@ZIF and (C) ZIF film (cross-sectional view) only. Scale bar, 200 nm. Comparison of the SERS performance of different platforms. The SERS intensities are obtained from the  $1002\text{ cm}^{-1}$  band of toluene.

## References

- [1] M. Mulvihill, A. Tao, K. Benjauthrit, J. Arnold, P. Yang, *Angew. Chem. Int. Ed.* **2008**, 47, 6456-6460.
- [2] G. Lu, J. T. Hupp, *J. Am. Chem. Soc.* **2010**, 132, 7832-7833.
- [3] Y. H. Lee, H. Chen, Q.-H. Xu, J. Wang, *The Journal of Physical Chemistry C* **2011**, 115, 7997-8004.
- [4] H. K. Lee, Y. H. Lee, I. Y. Phang, J. Q. Wei, Y. E. Miao, T. X. Liu, X. Y. Ling, *Angew. Chem. Int. Ed.* **2014**, 53, 5054-5058.
- [5] S. Lagergren, *Kungliga Svenska Vetenskapsakademiens. Handlingar* **1898**, 24, 1 - 39.
- [6] R. Kodiyath, S. T. Malak, Z. A. Combs, T. Koenig, M. A. Mahmoud, M. A. El-Sayed, V. V. Tsukruk, *Journal of Materials Chemistry A* **2013**, 1, 2777-2788.
- [7] D. O. B. Zenz C., Horvath EP Jr., *Occupational Medicine*, 3 ed., MO: Mosby-Year Book, Inc., St. Louis, **1994**.